

RESEARCH ARTICLE

Design framework for programmable mechanical metamaterial with unconventional damping properties under dynamic loading conditions

William Kaal^{1*}, Michael M. Becker², Marius Specht³ and Sarah C.L. Fischer²

¹Structural Dynamics and Vibration Technology, Fraunhofer Institute for Structural Durability and System Reliability LBF, Darmstadt, Germany.

²Fraunhofer Institute for Nondestructive Testing IZFP, Saarbrücken, Germany.

³Fraunhofer Institute for Mechanics of Materials IWM, Freiburg, Germany.

*Author for correspondence: William Kaal, Email: william.kaal@lbf.fraunhofer.de

Received: 12 August 2022; Accepted: 24 November 2022

Keywords: programmable materials; mechanical metamaterials; damping; energy absorption; customised material design

Abstract

A theoretical and experimental framework for novel metamaterial with programmable damping properties is presented. This material system is able to switch between elastic-dominated and damping-dominated regimes with different overall stiffness under dynamic loading depending on the external stimulus. The unit cell combines an auxetic and a bellow-like layer separated by an interface through which the amount of media flow can be tuned depending on the lateral strain. A simplified analytical model is derived to analyse the programmable damping effect. The model is further extended with a fluid-dynamics approach to link the effective damping properties with geometrical parameters to aid with the practical design of the metamaterial. Afterward, experiments are conducted on a macroscopic level using laser-sintered unit cells to validate the functionality of the concept both with air and water as media within the unit cells. To conclude the work, initial results on microscopic-level unit cells fabricated by two-photon lithography are introduced to showcase the scalability of the concept. This work provides an experimentally validated theoretical framework for future investigations to design unit cells with programmable damping on different length scales for applications requiring tailored dynamic energy dissipation.

Contents

Introduction	2
Results	3
Concept of damping metamaterial	3
Analytical mechanical model	3
Fluid-mechanics model	5
Mechanical testing: Air-filled system and effect of lateral strain	6
Mechanical testing: Fluid-filled system	8
Microscopic fluid-filled system	9
Discussion	10
Conclusion and outlook	11
Experimental section and methods	12
Manufacturing of macroscopic prototypes	12
Manufacturing of microscopic prototypes	12

Mechanical testing	12
Numerical simulations	12
References	13

Introduction

Dynamic loads represent a particular challenge for all materials and technical problems. Technical materials are only suitable for a narrow range of applications with regard to the compromise between mechanical stability, adaptability to the dynamic load and the service life of the component (Zhou et al., 2016). The macroscopic dynamic stiffness and damping properties of the materials directly influence the function, comfort, acoustic emission and precision of movements and are therefore ubiquitous in the design process (Barton and Fieldhouse, 2018; Baz, 2019). The associated requirements for systems with optimised properties under dynamic loads exceed the functionality that classical material properties offer (Corsaro and Sperling, 1990; Zhao et al., 2018; Menard and Menard, 2020), and therefore other approaches have to be investigated.

Materials with adaptive damping properties have been studied in the area of smart materials, for example, shape-memory alloys such as NiTi or magnetorheological fluids (MRF) (Carlson and Jolly, 2000; Zschunke, 2005; Zschunke et al., 2005; Olabi and Grunwald, 2007; Ahamed et al., 2018; Park et al., 2019) in which external stimuli such as temperature or a magnetic field are used to tune the properties. A wide variety of application fields have been considered for smart material-based components, ranging from civil engineering and the automotive industry to prosthetics and household appliances. (Sadeghipour et al., 1992; Meyer et al., 1998; Tzou et al., 2004) However, smart actuators and dampers are structurally complex systems that require an external control and an energy source for operation (Pishvar and Harne, 2020).

To realise adaptive damping properties without these limitations, integrating the geometrical design of a component as design parameter has shown promise in the area of mechanical metamaterials (Berwind et al., 2018; Lincoln et al., 2019; Surjadi et al., 2019; Fischer et al., 2020). This class of materials is based on unit cells that form artificial composites with unusual properties (Wang et al., 2016; Berwind et al., 2018; Mukhopadhyay et al., 2020). The unit cells are designed with tailored mechanical elements inside the material and concepts for potential applications such as high energy shock absorbers (Morris et al., 2019; Chen et al., 2020) or specific acoustic properties have been published (Yang et al., 2010; Bückmann et al., 2012; Manimala and Sun, 2014; Cummer et al., 2016; Frenzel et al., 2016; Zhang et al., 2021).

Based on these design principles, researchers have further investigated strategies to implement logic into the system in so-called programmable metamaterials (Berwind et al., 2018). The goal is to design material systems exhibiting drastically different mechanical response or even enable several metastable states depending on the external stimuli the material system is subjected to. Concepts currently range from utilisation of contact effects of internal surfaces in microstructures (Hewage et al., 2016; Li et al., 2020) to integrating electromagnets to switch between several configurations (Haghpanah et al., 2016; Wang et al., 2016) and are expanded rapidly by many international research groups. However, the main focus of these publications is the change of static or quasi-static metastable behaviour.

Programmable metamaterials with a special focus on dynamic damping effects have not been extensively studied yet. Therefore, this article proposes, for the first time, a design framework for programmable mechanical metamaterials with varying damping properties depending on an external lateral strain as an intrinsic property of a single-material system. The goal is to design an internal structure capable of changing the working areas of the programmed material reversibly to enable switching between different states during operation. The trigger that is focused on in this work is the mechanical strain, which is actively changed by an external mechanical force and can in the future be passively changed using temperature effects using shape-memory polymers. In this way, mechanical metamaterials which change their dynamic properties according to specific needs without complex electronical infrastructure can be designed.

Results

Concept of damping metamaterial

In order to establish a framework for the design of material systems with programmable damping properties, a fundamental design for a unit cell was established. The unit cell consists of a combination of two functional layers (Figure 1). The first layer consists of a flexible sealed cavity, here a bellow, with an orifice at the interface to the second layer. This first layer provides the elasticity of the material and the damping effect in one direction. The bottom layer consists of an auxetic porous structure, which expands in the vertical direction by a lateral strain. Through the vertical expansion of the structure, an integrated plug is lifted, which opens the orifice and thus serves as an openable valve for the cavity. Therefore, the bottom layer provides the trigger functionality of the material system to switch between states with different damping and stiffness.

This parametric model enables the material systems to trigger functionality, the stiffness as well as frequency-dependent damping properties to be customised depending on the requirements of the application (Figure 1b). In the next sections, two complementary numerical models to optimise the structures will be introduced and subsequently validated by experiments.

Analytical mechanical model

To design and analyse the general behaviour of a unit cell, a simplified mechanical model of the bellow layer is established as shown in Figure 2. It comprises the bellow, characterised by its height h , its diameter d (defining the cross-sectional area A), its inherent stiffness k , its inherent damping value b and its blowing rigidity c , which can also, as a first approximation, be used to include the compressibility of the fluid (Figure 2a).

The state of the orifice of the bellow is described by the parameter s , which quantifies the fluid flow at a certain internal pressure p . Small values of s thus describe an almost fully closed valve, whereas large values of s describe an open valve. The model is excited by an external harmonic force F over time t at a certain frequency f and the elongation x over time t is evaluated regarding the excitation, yielding a dynamic stiffness and a loss angle for each configuration.

The deformation behaviour of the bellow can be described in a first approximation using two equations:

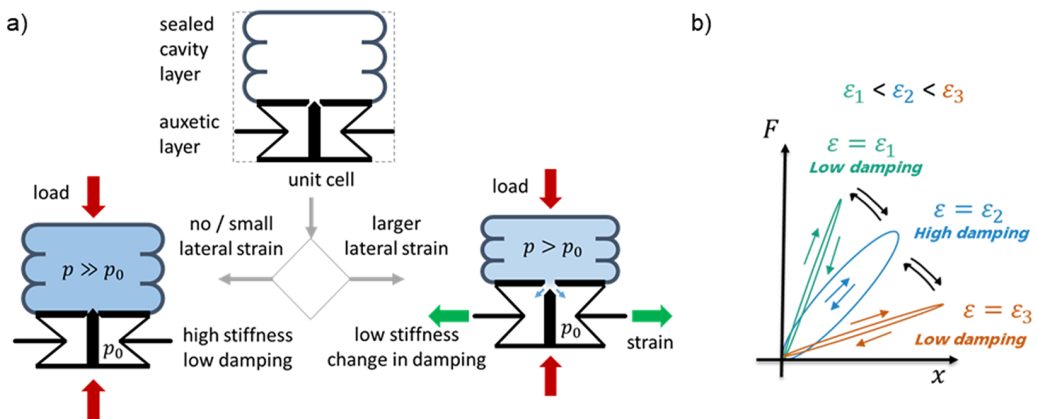


Figure 1. Implementation of a programmable damping effect in microstructure based on unit cells. (a) Basic design of a unit cell with two functional layers, the sealed cavity or bellow layer (blue, top) and the auxetic layer (black, bottom). (b) Schematic of the different regimes that can be programmed into the material system.

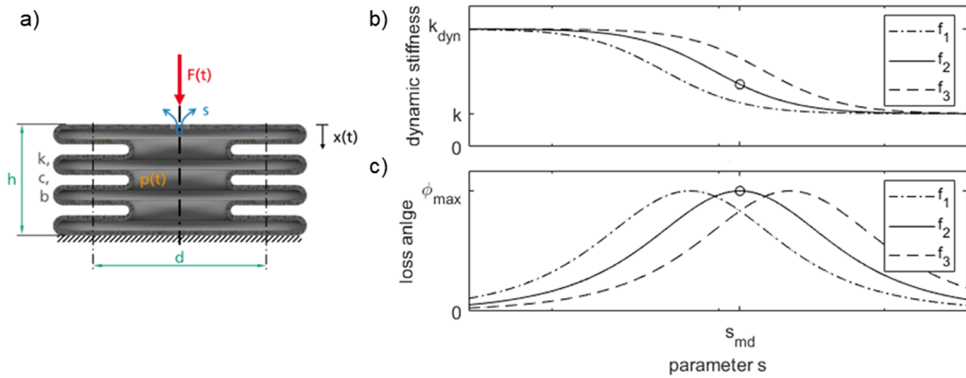


Figure 2. Analytical model for the programmable damping material. (a) Schematic of the bellow layer with characteristic parameters for analytical model. Frequency-dependent results of dynamic stiffness (b) and loss angle (c) over orifice opening represented by fluid flow factor s .

$$F(t) = A p(t) + k x(t) + b \dot{x}(t), \tag{1}$$

$$A x(t) = \frac{1}{c} p(t) + \int s p(t) dt. \tag{2}$$

Equation (1) describes the normal equilibrium of force at the point of load application. The input force is opposed to the sum of the forces resulting from the mechanics of the bellow itself, that is, its stiffness and damping properties, and the current internal pressure acting on the cross-sectional area A .

Equation (2) describes the fluid volume inside the bellow, considering both its blowing rigidity c and the fluid flow through the valve, assuming that the fluid flow is proportional to the internal pressure p and the parameter s . The internal pressure p is defined as the relative internal pressure compared to the ambient pressure, therefore in the unloaded case p equals 0.

Assuming harmonic behaviour of all time-dependent values with frequency f and amplitude values of \hat{x} , \hat{p} , and \hat{F} , respectively in complex notation yields equation (3) for the dynamic stiffness of the system by dividing the force amplitude by the stroke amplitude:

$$k_{\text{dyn}} = \frac{\hat{F}}{\hat{x}} = k + \frac{A^2}{\frac{1}{c} + \frac{s}{i2\pi f}} + i2\pi f b. \tag{3}$$

From this equation, the maximum static stiffness is reached for a fully closed valve ($s = 0$) and is given by

$$k_{\text{dyn,max}} = A^2 c + k, \tag{4}$$

whereas the minimum static stiffness is reached for a fully open valve ($s \rightarrow \infty$) and is given by

$$k_{\text{dyn,min}} = k. \tag{5}$$

The damping of the system can be characterised by the loss angle φ , which is the angle between force and stroke, and it can be calculated in the following way:

$$\tan \varphi = \frac{Ac^2s\omega + bc^2s^2\omega + b\omega^3}{A^2c\omega^2 + k\omega + kc^2s^2}. \tag{6}$$

Assuming the material damping characterised by the parameter b can be neglected compared to the fluidic damping effect, the maximum loss angle φ can be mathematically determined by equating its

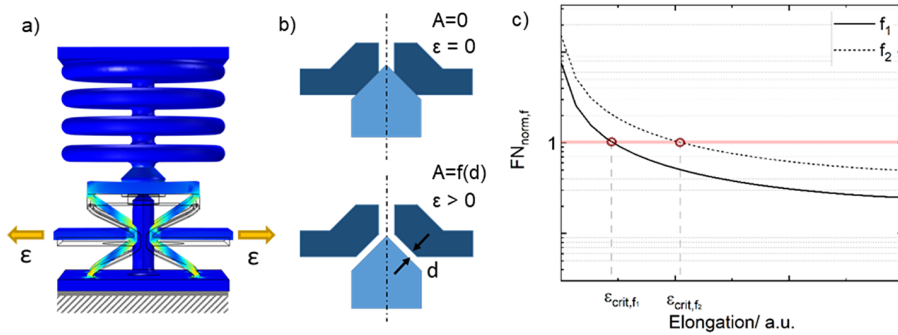


Figure 3. Fluid-based model to predict the critical strain for different frequencies based on numeric simulations of the unit cell. (a) FEM model to simulate the strain-dependent cross-section for a specific parametrised unit cell. (b) Visualisation of the cross-section for $\epsilon = 0$ and $\epsilon > 0$. (c) Qualitative results of the fluid-mechanics prediction for the flow number $FN_{norm,f}(\epsilon)$ at two different frequencies.

first derivative to 0, leading to the value of s at which the highest damping occurs

$$s_{\max\text{damp}} = \frac{\omega}{c} \sqrt{\frac{A^2 c + k}{k}} = \frac{\omega}{c} \sqrt{\frac{k_{\text{dyn,max}}}{k_{\text{dyn,min}}}}. \quad (7)$$

The maximum damping can therefore be achieved for large stiffness ratios. The resulting maximum loss angle can be calculated in the following way:

$$\varphi_{\max} = \tan^{-1} \left(\frac{1}{2} \frac{\frac{A^2 c + k}{k} - 1}{\sqrt{\frac{A^2 c + k}{k}}} \right). \quad (8)$$

Exemplary curves of the dynamic stiffness and loss angle according to the above model are shown in Figure 2b,c to visualise the influence of the frequency and shifts of $s_{\max\text{damp}}$. The shape of the stiffness versus frequency curve is similar for all excitation frequencies and exhibits two distinct regimes for extreme values of s , converging toward $k_{\text{dyn,min}}$ for the fully open and $k_{\text{dyn,max}}$ for fully closed system. However, a lateral shift of the transition toward larger values of s is observed with increasing frequency.

The loss angle reaches a maximum φ_{\max} independently of the excitation frequency. The position of the peak of the loss angle $s_{\max\text{damp}}$ shifts to higher values of s with increasing excitation frequency.

Fluid-mechanics model

Based on the previous model, the critical fluid flow $s_{\max\text{damp}}$ can be used as a design parameter. However, in practice, this parameter is not accessible as it is dependent on the material topography and cannot be directly correlated to the magnitude of the lateral strain required. Therefore, besides the numerical model that can be used to make the principal design of the damping unit cells, we propose a practical approach based on fluid dynamics combined with a FEM simulation (Figure 3). It is used to determine the experimental shifts of the maximum damping depending on the frequency and the lateral strain and predict the lateral strains with maximum damping behaviour at a certain frequency.

Fluid flow is usually described by the Reynold's number Re .

$$Re = \frac{\rho \cdot v \cdot s_{\text{char}}}{\mu}. \quad (9)$$

The Reynold's number is a function of the density of the fluid ρ , the viscosity of the fluid μ , the fluid flow speed v , the cross-sectional area A and the characteristic linear dimension s_{char} . In the case of a programmable unit cell, the fluid flow speed is defined as

$$v = \frac{\dot{V}}{A(\varepsilon)} = \frac{V_{norm} \cdot f}{A(\varepsilon)}. \quad (10)$$

where \dot{V} is the volume flow per time increment and is proportional to the frequency. The cross-sectional area A is a function of the lateral strain ε and is characteristic of a unit cell and the central design parameter.

In this work, we define a flow number FN proportional to the Reynold's number.

$$FN_f(\varepsilon) = \frac{1}{A(\varepsilon)} f \propto Re. \quad (11)$$

The characteristic flow number for a unit cell can be determined by analysing the damping behaviour of a unit cell experimentally and measuring the critical lateral strain ε_{crit,f_0} for which damping is highest at a frequency f_0 . Normalising the flow number by $FN_{f_0}(\varepsilon_{crit,f_0})$ yields a design criterion for the strain at different frequencies.

$$FN_{norm,f}(\varepsilon) = \frac{1}{A(\varepsilon)} \cdot f \cdot \frac{1}{FN_{f_0}(\varepsilon_{crit,f_0})}. \quad (12)$$

$A(\varepsilon)$ depends on the design parameters of the unit cell and thus has to be computed using a time-dependent FEM simulation (Figure 3a,b). As shown in Figure 3c, the flow number $FN_{norm,f}(\varepsilon)$ can be plotted as a function of ε as long as the relationship between A and ε is known. For target frequencies f_n the normalised flow number FN_{norm,f_n} needs to be close to 1 to reach maximum damping properties and determine the ε_{crit,f_n} .

The two previous models provide the tools to design a unit cell with programmable damping properties. They represent simplified models and cannot quantitatively predict the damping behaviour without any experiments, but still narrow down the design space and thus drastically reduce the development time for new applications.

Mechanical testing: Air-filled system and effect of lateral strain

The following sections showcase the functionality of exemplary unit cells and serve as validation for the aforementioned models. To validate the results from the numerical models, unit cells were fabricated using selective laser sintering (Figure 4). Mechanical experiments were performed under different loading conditions while the unit cells were subject to varying boundary conditions.

First, only the bellow was excited by a 2 mm stroke at 1 Hz in two different states: with a completely open valve and with a completely closed valve using a wax seal. The force response was monitored over the course of 10 cycles to determine the equivalents of k_{dyn} and $k_{dyn,max}$ from the mechanical model. A preload of 0.19 N was used to guarantee contact between the structure and the testing machine at all times. The hysteresis is narrow in both cases which means the damping is low. The stiffness of the unit cell is approximated based on a linear fit, $k_{dyn,max}$ and k_{dyn} (cf. Figure 1), corresponding to a factor of about 3.5 increase in the stiffness. In both cases, the system response showed a small settling effect but stabilised after a few cycles. This showcases the general ability of the unit cell to cover a wide range of stiffness based on the lateral strain trigger (cf. Figure 1b).

To further describe the effects of the lateral strain trigger, one exemplary unit cell was modified with a further coating to smooth the surface roughness and was meticulously positioned in the tensile testing machine to qualitatively analyse the expected effects. The results are displayed in Figure 5 at a

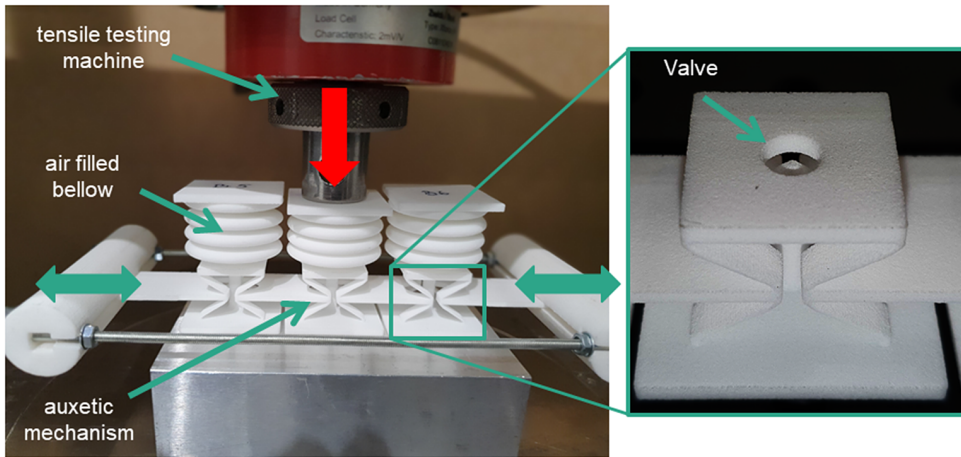


Figure 4. Test rig with macroscopic programmable damping material with three unit cells in a row. The testing was performed with an excitation of 2 mm stroke at 1 Hz.

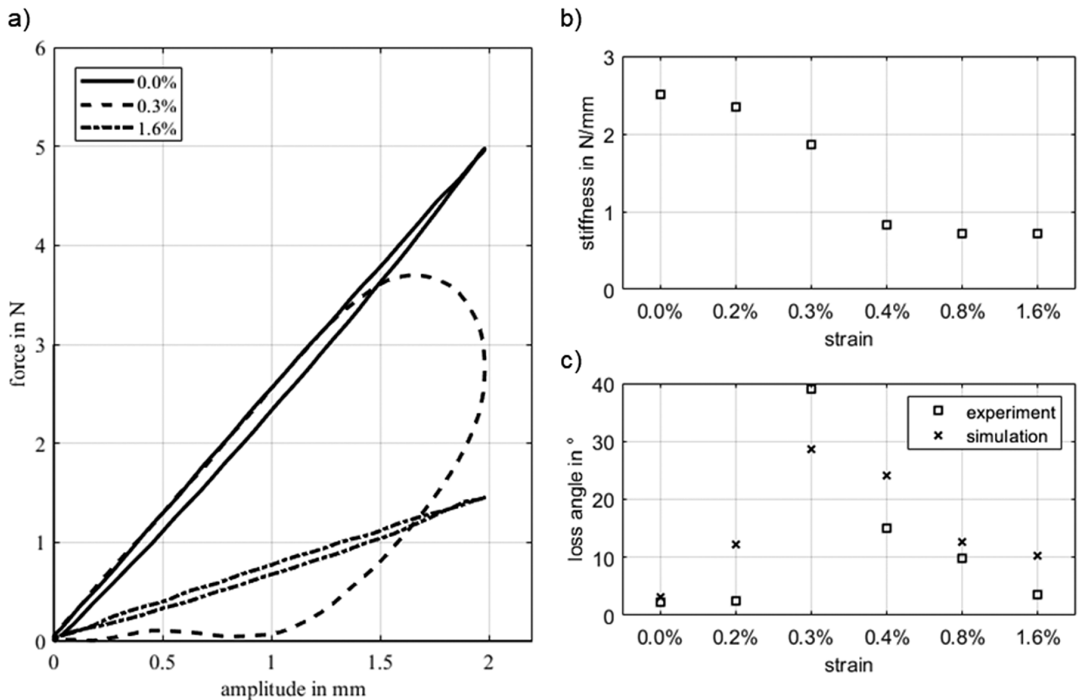


Figure 5. Measurement results of one exemplary macroscopic unit cell at different strains. (a) Force/stroke diagram for different strain conditions, steady state at 1 Hz. (b) Evaluation of linearised stiffness for different strain conditions. (c) Evaluation of loss angle for different strain conditions (squares) and results from the numerical model (crosses).

measurement rate of 1 Hz. The shape of the force-displacement curves within one deformation cycle strongly varied depending on the strain (Figure 5a). For both small and large strains, the loading and unloading curves are fairly linear with small hysteresis and the stiffness values are in good agreement with the results presented in the previous section. For intermediate strains of around 0.3%, the loading and unloading slopes are distinctly different and nonlinear, resulting in a large hysteresis (Figure 5a).

Table 1. Comparison of experimental and numerical data for one exemplary macroscopic unit cell at different strains as shown in Figure 5b,c

Strain (%)	Stiffness from experiments (N/mm)	Factor s for simulations at 1 Hz	Loss angle from simulations (°)	Loss angle from experiment (°)
0	2.51	5.5e-11	2.36	3.2
0.2	2.34	2.2e-10	2.44	12.2
0.3	1.87	6.8e-10	39.0	28.7
0.4	0.84	3.6e-9	15.0	24.1
0.8	0.73	8.0e-9	9.81	12.6
1.6	0.72	1.0e-8	3.46	10.2

To evaluate the phenomenon quantitatively, the stiffness of the system is calculated using a linear fit between the minimum and maximum values of force and stroke whereas the loss angle is calculated using the hysteresis area H , using the formula given in equation (13):

$$\varphi = \arcsin \left(\frac{4H}{\pi} \frac{1}{\max(F) - \min(F)} \frac{1}{\max(x) - \min(x)} \right). \quad (13)$$

The stiffness of the system decreases with increasing strain from 2.5 to 0.7 N/mm between 0 and 0.8% strain (Figure 5b). For strains above 0.8%, the stiffness plateaued at around 0.7 N/mm. The damping angle exhibited a bell-shaped curve with a peak value of around 38° at 0.3% strain with values close to 3° for strains of 0 and 0.2% and loss angles from 15° down to 5° for strains from 0.4% up to 1.6%.

To contrast the results from experiments and the mechanical model, the loss angle was derived from the mechanical model based on a set of parameters mimicking the macroscopic experimental demonstrator: $h = 18$ mm, $d = 24$ mm, $b = 0.3$ Ns m⁻¹, $k = 0.7$ N/mm, $c = 0.88$ N/cm⁵ (cf. Figure 2a). The experimentally determined stiffnesses k_{dyn} were used to calibrate the model and determine the flow factors s from simulations that are expected for the different strains (Table 1). For these flow factors s , both experimental and simulation data of the loss angle for an excitation frequency of 1 Hz are compared in Figure 5c. Experimental results and numerical predictions show a similar trend with a maximum in the loss angle between 0.2 and 0.4% strain. Deviations in the absolute values are observed especially around the peak which is likely caused by experimental inaccuracies in the manufacturing and alignment of the specimens.

Preliminary experiments showed that the trigger position and behaviour of air-filled unit cells are qualitatively in agreement with the models. However, manufacturing variations caused by the SLS process have a strong impact on the surface roughness and therefore the airflow within the cavities. Introducing water to the cells improved this and enabled carrying out experiments with a system of three unit cells to study the frequency-dependent behaviour in the next section.

Mechanical testing: Fluid-filled system

Additional mechanical experiments were performed on three parallel unit cells submerged in water to obtain an incompressible medium in the unit cell (Figure 6) to showcase the frequency-dependent behaviour of the unit cells. Figure 6a shows the force-displacement curves of the samples between 0 and 3% strain at 1 Hz with the same characteristic behaviour as previously observed for air-filled unit cells. The dynamic stiffness increased due to the addition of water and varied between 10 N/mm for low strains and 2.5 N/mm at high strains which corresponds to a 4-fold change in stiffness. An increase in the area of the hysteresis and loss angle was observed at about 1% strain for 1 Hz.

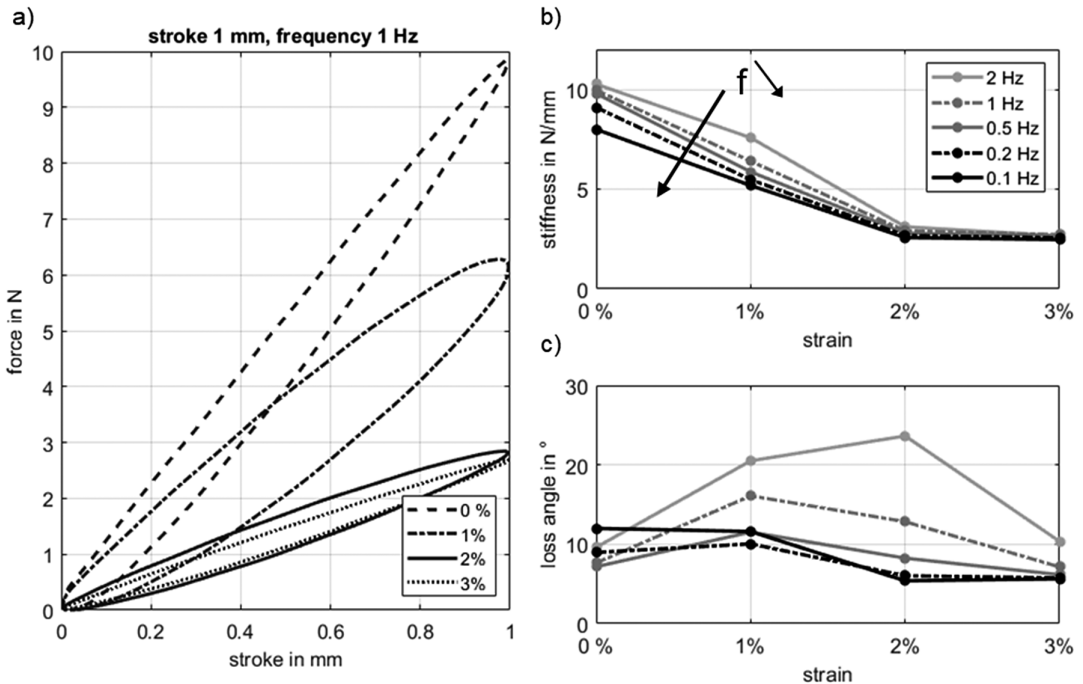


Figure 6. Measurement results of three macroscopic unit cells filled with water at different strains. (a) Force/stroke diagram for different strain conditions, steady state at 1 Hz. (b) Evaluation of linearised stiffness for different strain conditions and different frequencies. (c) Evaluation of loss angle for different strain conditions and different frequencies.

Measurements were repeated at frequencies of 2, 1 and 0.2 Hz and the dynamic stiffness, as well as loss angle, were analysed (Figure 6b,c). The dynamic stiffness decreases with increasing strain for all frequencies. It could be observed that the transition to the lower stiffness plateau $k_{\text{dyn,min}}$ is shifted toward lower strains with lower frequencies which is in good agreement with the mechanical model. The loss angle exhibits a peak between 0 and 2% strain for all frequencies. A shift of the peak position to lower strains can be observed although the quantitative analysis of the peaks is challenging as the strain increments are quite large and the differences in the behaviour below 0.5 Hz are small. At 0.1 Hz it is not clear whether there is a maximum at all in this strain regime.

For validation of the fluid mechanics model, the cross-sectional area of the unit cells as a function of strain was calculated using a finite element study and the flow numbers $\text{FN}_{\text{norm},f}(\varepsilon)$ calculated and plotted in Figure 7. The frequency of 2 Hz was chosen as the reference and therefore, based on experimental results, the flow numbers normalised so that $\text{FN}_{2\text{Hz}}(2\%) = 1$. The fluid mechanics model predicts decreasing $\varepsilon_{\text{crit},f_n}$ with decreasing frequency f_n to be $\varepsilon_{\text{crit},1\text{Hz}} \sim 1.1\%$, $\varepsilon_{\text{crit},0.5\text{Hz}} \sim 0.5\%$, $\varepsilon_{\text{crit},0.2\text{Hz}} \sim 0.1\%$ and $\varepsilon_{\text{crit},0.1\text{Hz}} < 0.1\%$. These results are in good agreement with the results from the experiments shown in Figure 6c.

Microscopic fluid-filled system

Scalability of the unit cell principle was demonstrated with unit cells manufactured by two-photon polymerisation (Figure 8). This technique enables manufacturing the unit cells in a single process and out of a single raw material. In this case, the unit cells were neither filled with air nor water due to the manufacturing process but contain nonpolymerised resin as a damping fluid.

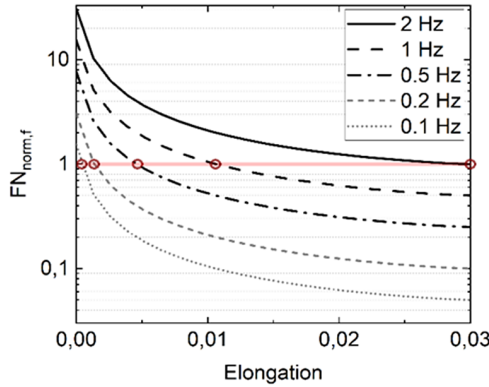


Figure 7. Predictions based on the fluid-mechanics model for different frequencies from 0.1 to 2 Hz.

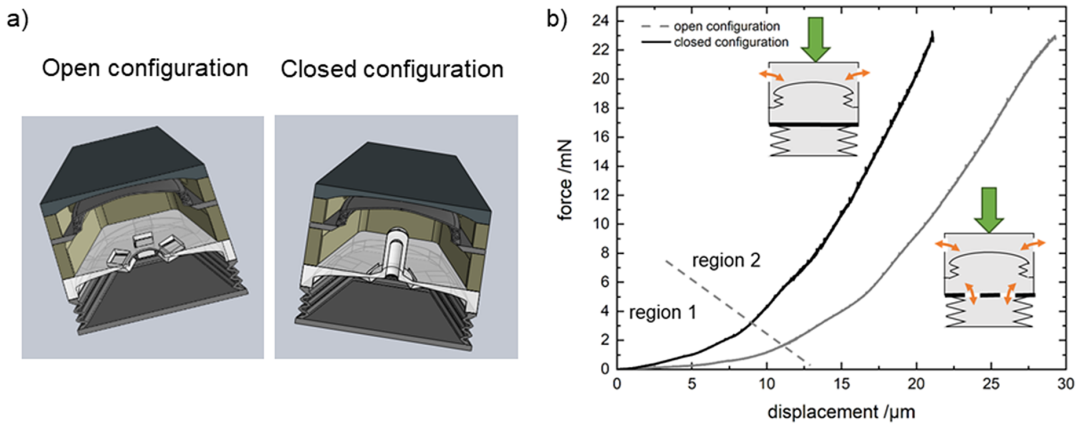


Figure 8. Microscopic proof of principle for damping unit cells. (a) Model of the two printed configurations and (b) results of microcompression tests of structures exhibiting two force regions.

Two different unit cell types were manufactured to mimic the macroscopic cells with two functional layers, either allowing or preventing fluid flow between the two layers (Figure 8a). Unit cells were arranged in arrays of three times three unit cells with a size of approximately $30 \times 30 \times 30 \mu\text{m}^3$ and all unit cells were tested at the same time. Compression experiments revealed highly nonlinear deformation behaviour for both unit cells (Figure 8b): The open unit cell was generally softer than the closed unit cell. Both curves qualitatively show two different regimes: For small deformations, the unit cells stiffness is linear over a small range of displacement and then transitions into a second regime with a higher slope at a similar force of about 2 μN . The open cell exhibits a slope of 0.06 $\text{mN}/\mu\text{m}$ in the first and 1.64 $\text{mN}/\mu\text{m}$ in the second regime. The closed cell exhibits a slope of 0.23 $\text{mN}/\mu\text{m}$ in the first and 2.01 $\text{mN}/\mu\text{m}$ in the second regime. Investigation of the structures before and after compression in an SEM revealed no significant plastic deformation of the cells.

The dynamic properties as well as the strain trigger were not investigated as part of this research work but will need to be explored in future experiments with more sophisticated unit cell designs and testing equipment.

Discussion

Programmable mechanical metamaterials vary their mechanical properties depending on the environmental conditions or their operating status. They have the potential to introduce a paradigm shift

in the handling of materials because they replace technical systems comprised of many components and materials with an individual, locally configured material. This allows for the implementation of complex and locally diverse effects which enable completely new component functions. In this article, we presented a new metamaterial design with programmable damping properties based on a strain trigger and were able to demonstrate its functionality through numerical models and experiments.

In a vertically loaded and laterally unstrained condition (valve completely closed), the bellow of the unit cell is compressed and the pressure inside increases. In this condition, the stiffness is specified by the combination of the structural bellow stiffness and the compressed medium stiffness. In a vertically loaded and laterally strained (valve completely opened) condition the medium inside the bellow can exhaust to the environment and the stiffness is mainly specified by the structural bellow stiffness, which will be lower than in the laterally unstrained condition (cf. [Figure 1](#)).

The experimental results revealed stiffness of about 2.49 N/mm for the closed configuration and 0.71 N/mm for an open configuration with air as a medium (cf. [Figure 5b](#)) and 10 N/mm and 2.5 N/mm, respectively, for water as a medium (cf. [Figure 6b](#)). The resulting magnitude of the loss angle variation and the position of the maximum can be predicted using the numerical model (cf. [Figure 5c](#)). Frequency-dependent damping behaviour was validated by experiments with the fluid-filled system (cf. [Figure 6c](#)). The fluid-mechanics model is in good agreement with the experiments (cf. [Figure 7](#)) and will serve as a design guideline for future applications where the target is to target specific resonant frequencies to be dampened. For these applications, the unit cell design will need to be further optimised to showcase sharper transitions between the regimes and a highly localised peak in damping.

In general, based on both the air-filled and fluid-filled unit cells, it was demonstrated that dynamic stiffness and damping properties of a polymeric metamaterial can be tailored based on the proposed design framework. With one single material, a nearly three-fold variation of the dynamic stiffness could be achieved, and a significant increase in the loss angle at one specific trigger point. While differences in damping are usually observed in polymers due to time-dependent material characteristics, the approach presented in this work enables tuning of these parameters independently of velocity based on the unit cell parameters. The numerical model established in this work was in very good agreement with the experimental results and can be used to establish design criteria for the unit cells for different applications in the future.

In principle, the presented mechanism can be scaled using different manufacturing approaches. In this article, we showed a proof-of-concept downscaling of the mechanism using two-photon lithography to reduce the dimension of one unit cell to the micrometre range. Compression experiments showed different behaviour comparing open and closed configurations. The compression curves exhibit two regimes. We assume that the first regime is dominated by deformation of the bellow and at a certain threshold force the deformation is more uniformly distributed throughout the unit cell and the top part of the unit cell starts to contribute to the stiffness which causes the increase.

While downscaling to the microscale might be interesting for high-precision applications, large-scale fabrication at the scale of the macroscopic unit cells is also interesting when thinking about industrial translation of the principles. Future work will need to investigate whether the unit cell design can be modified to enable high-throughput methods such as extrusion processes or lamination processes.

Conclusion and outlook

The current study proposes a new concept of programmable metamaterials that feature damping effects beyond conventional bulk materials. The damping is caused by dissipative fluid flow within the geometrical features of the material. The dynamic damping properties of the metamaterial can be programmed to vary with the external strain, creating a new degree of freedom in the material design. The stiffness and damping depend on the different ratios of the structural bellow, the valve orifice and the auxetic strain mechanism and can be tuned for specific applications.

The implementation of this new type of structure–property coupling in commercial applications encompasses major challenges since these are solutions that require tailoring to a specific set of

functionalities. Exploring the present design framework and adapting it to specific applications will require more research effort in various areas. The scalability of the concept, both on the macroscopic scale as well as on a smaller scale, is challenging and requires modifications of the design framework. Approaches for quality assurance will also need to be addressed in the future as they are crucial for any engineering application.

The design framework for programmable mechanical metamaterials with unconventional damping properties under dynamic loading conditions presented is thought as a basis for further research to build upon and extend and will hopefully inspire many interesting applications for metamaterials in the coming years.

Experimental section and methods

Manufacturing of macroscopic prototypes

Macroscopic unit cells were designed and built up via additive manufacturing in SLS (Selective Laser Sintering) process (EOSINT P395) (cf. [Figure 3](#)). Polyamide (PA12) was chosen as the material due to its suitable mechanical properties (breaking elongation > 18%, Young's modulus 1,650 MPa). The unit cells were manufactured in two layers, a bellow layer and an auxetic layer, and subsequently assembled with glue (LOCTITE 401). Each macroscopic unit cell has a size of approx. $30 \times 30 \times 40 \text{ mm}^3$.

Manufacturing of microscopic prototypes

The microscopic unit cell samples were fabricated with a commercially available two-photon lithography system (Nanoscribe Photonic Professional GT, by Nanoscribe GmbH, Germany) using liquid negative-tone photoresist (IP-Dip) and a $63\times$ oil objective with Numerical Aperture of 1.4 by Carl Zeiss AG, Germany. The resist was solidified via two-photon polymerisation (2PP) using a frequency-doubled 780 nm fibre laser with 100 fs pulses, 50 mW power and 10 000 $\mu\text{m/s}$ speed.

Before the writing process, silicon substrates were plasma etched with 2 kW power under $50 \text{ cm}^3/\text{min}$ air pressure for 5 min to enhance the adhesion of the acryl-based resist to the polymer substrates.

After the 2PP process, the samples were developed and cleaned in PGMEA for 30 min (solvent from Sigma-Aldrich) and subsequently washed in isopropyl alcohol with additional UV-light exposure for 5 min to enhance polymerisation.

Mechanical testing

Macroscopic mechanical testing was performed in a uniaxial testing machine manufactured by ZwickRoell (BT1-FR10THW.A50). During the tests, the ram presses on the bellow, and stroke and force are measured simultaneously. A custom-built fixture with two threaded rods and nuts is used to adjust the straining for testing.

The microscopic unit cells were characterised in a custom-built uniaxial indentation machine with a flat punch indentation tip. Therefore, a pattern of 3×3 unit cells was compressed stepwise with a stress-controlled computer-guided program, while the responsive forces were measured with a sensitive load cell. For additional visual control and guidance, a CCD Camera System was added in front of the indentation tip. To evaluate the compression of the microscopic unit cell, the samples were analysed in a scanning electron microscope (SEM) before and afterward.

Numerical simulations

The numerical simulations of the unit cell were performed using Comsol Multiphysics (version 5.4). The 3D models studied are identical to the data used for the production of the unit cell. The deformation

was applied in a quasi-stationary simulation. All components were approximated with an isotropic linear elastic material model assuming small local deformations.

Data availability statement. Data sharing is not applicable to this article.

Financial support. This work was partially supported by the Fraunhofer Cluster of Excellence ‘Programmable Materials’. S.C.L.F. acknowledges funding from the Fraunhofer Internal Programs under Grant No. Attract 025-601314.

Competing Interest. The authors declare no competing interests exist.

References

- Ahamed R, Choi S-B and Ferdous MM** (2018) A state of art on magneto-rheological materials and their potential applications. *Journal of Intelligent Material Systems and Structures*, **29**(10), 2051–95. DOI:[10.1177/1045389X18754350](https://doi.org/10.1177/1045389X18754350).
- Barton DC and Fieldhouse JD** (2018). Noise, Vibration and Harshness (NVH). In *Automotive Chassis Engineering*, **Barton DC and Fieldhouse JD** (eds.), 255–317. Cham: Springer International Publishing.
- Baz AM** (2019) *Active and Passive Vibration Damping*. Somerset: John Wiley & Sons Incorporated. <https://ebookcentral.proquest.com/lib/kxp/detail.action?docID=5613314>
- Berwind MF, Kamas A and Eberl C** (2018) A Hierarchical Programmable Mechanical Metamaterial Unit Cell Showing Metastable Shape Memory. *Advanced Engineering Materials*, **20**(11), 1800771. DOI:[10.1002/adem.201800771](https://doi.org/10.1002/adem.201800771).
- Bückmann T, Stenger N, Kadic M, Kaschke J, Frölich A, Kennerknecht T, Eberl C, Thiel M and Wegener M** (2012) Tailored 3D mechanical metamaterials made by dip-in direct-laser-writing optical lithography. *Advanced materials (Deerfield Beach, Fla.)*, **24**(20), 2710–14. DOI:[10.1002/adma.201200584](https://doi.org/10.1002/adma.201200584).
- Carlson J and Jolly MR** (2000) MR fluid, foam and elastomer devices. *Mechatronics*, **10**(4-5), 555–69. DOI:[10.1016/S0957-4158\(99\)00064-1](https://doi.org/10.1016/S0957-4158(99)00064-1).
- Chen X, Ji Q, Wei J, Tan H, Yu J, Zhang P, Laude V and Kadic M** (2020) Light-weight shell-lattice metamaterials for mechanical shock absorption. *International Journal of Mechanical Sciences*, **169**, 105288. DOI:[10.1016/j.ijmecsci.2019.105288](https://doi.org/10.1016/j.ijmecsci.2019.105288).
- Corsaro RD and Sperling LH** (1990) *Sound and Vibration Damping with Polymers*. Washington, DC: American Chemical Society.
- Cummer SA, Christensen J and Alù A** (2016) Controlling sound with acoustic metamaterials. *Nature Reviews Materials*, **1**(3). DOI:[10.1038/natrevmats.2016.1](https://doi.org/10.1038/natrevmats.2016.1).
- Fischer SCL, Hillen L and Eberl C** (2020) Mechanical Metamaterials on the Way from Laboratory Scale to Industrial Applications: Challenges for Characterization and Scalability. *Materials (Basel, Switzerland)*, **13**(16). DOI:[10.3390/ma13163605](https://doi.org/10.3390/ma13163605).
- Frenzel T, Findeisen C, Kadic M, Gumbsch P and Wegener M** (2016) Tailored Buckling Microlattices as Reusable Light-Weight Shock Absorbers. *Advanced materials (Deerfield Beach, Fla.)*, **28**(28), 5865–70. DOI:[10.1002/adma.201600610](https://doi.org/10.1002/adma.201600610).
- Haghpanah B, Ebrahimi H, Mousanezhad D, Hopkins J and Vaziri A** (2016) Programmable Elastic Metamaterials. *Advanced Engineering Materials*, **18**(4), 643–49. DOI:[10.1002/adem.201500295](https://doi.org/10.1002/adem.201500295).
- Hewage TAM, Alderson KL, Alderson A and Scarpa F** (2016) Double-Negative Mechanical Metamaterials Displaying Simultaneous Negative Stiffness and Negative Poisson’s Ratio Properties. *Advanced materials (Deerfield Beach, Fla.)*, **28**(46), 10323–32. DOI:[10.1002/adma.201603959](https://doi.org/10.1002/adma.201603959).
- Li D, Gao R, Dong L, Lam W-K and Zhang F** (2020) A novel 3D re-entrant unit cell structure with negative Poisson’s ratio and tunable stiffness. *Smart Materials and Structures*, **29**(4), 45015. DOI:[10.1088/1361-665X/ab6696](https://doi.org/10.1088/1361-665X/ab6696).
- Lincoln RL, Scarpa F, Ting VP and Trask RS** (2019) Multifunctional composites: a metamaterial perspective. *Multifunctional Materials*, **2**(4), 43001. DOI:[10.1088/2399-7532/ab5242](https://doi.org/10.1088/2399-7532/ab5242).
- Manimala JM and Sun CT** (2014) Microstructural design studies for locally dissipative acoustic metamaterials. *Journal of Applied Physics*, **115**(2), 23518. DOI:[10.1063/1.4861632](https://doi.org/10.1063/1.4861632).
- Menard KP and Menard NR** (2020) *Dynamic Mechanical Analysis*. Boca Raton, FL: CRC Press.
- Meyer JL, Harrington WB, Agrawal BN and Song G** (1998) Vibration suppression of a spacecraft flexible appendage using smart material. *Smart Materials and Structures*, **7**(1), 95–104. DOI:[10.1088/0964-1726/7/1/011](https://doi.org/10.1088/0964-1726/7/1/011).
- Morris C, Bekker L, Spadaccini C, Haberman M and Seepersad C** (2019) Tunable Mechanical Metamaterial with Constrained Negative Stiffness for Improved Quasi-Static and Dynamic Energy Dissipation. *Advanced Engineering Materials*, **21**(7), 1900163. DOI:[10.1002/adem.201900163](https://doi.org/10.1002/adem.201900163).
- Mukhopadhyay T, Ma J, Feng H, Hou D, Gattas JM, Chen Y and You Z** (2020) Programmable stiffness and shape modulation in origami materials: Emergence of a distant actuation feature. *Applied Materials Today*, **19**, 100537. DOI:[10.1016/j.apmt.2019.100537](https://doi.org/10.1016/j.apmt.2019.100537).
- Olabi AG and Grunwald A** (2007) Design and application of magneto-rheological fluid. *Materials & Design*, **28**(10), 2658–64. DOI:[10.1016/j.matdes.2006.10.009](https://doi.org/10.1016/j.matdes.2006.10.009).
- Park J, Kim HM, Youn JR and Song YS** (2019) Smart Noise Control Using Shape Memory Sound Absorber. *Advanced Materials Technologies*, **4**(2), 1800410. DOI:[10.1002/admt.201800410](https://doi.org/10.1002/admt.201800410).

- Pishvar M** and **Harne RL** (2020) Foundations for Soft, Smart Matter by Active Mechanical Metamaterials. *Advanced science (Weinheim, Baden-Württemberg, Germany)*, **7**(18), 2001384. DOI:[10.1002/advs.202001384](https://doi.org/10.1002/advs.202001384).
- Sadeghipour K**, **Salomon R** and **Neogi S** (1992) Development of a novel electrochemically active membrane and ‘smart’ material based vibration sensor/damper. *Smart Materials and Structures*, **1**(2), 172–79. DOI:[10.1088/0964-1726/1/2/012](https://doi.org/10.1088/0964-1726/1/2/012).
- Surjadi JU**, **Gao L**, **Du H**, **Li X**, **Xiong X**, **Fang NX** and **Lu Y** (2019) Mechanical Metamaterials and Their Engineering Applications. *Advanced Engineering Materials*, **21**(3), 1800864. DOI:[10.1002/adem.201800864](https://doi.org/10.1002/adem.201800864).
- Tzou HS**, **Lee H-J** and **Arnold SM** (2004) Smart Materials, Precision Sensors/Actuators, Smart Structures, and Structronic Systems. *Mechanics of Advanced Materials and Structures*, **114**(5), 367–93. DOI:[10.1080/15376490490451552](https://doi.org/10.1080/15376490490451552).
- Wang X-T**, **Li X-W** and **Ma L** (2016) Interlocking assembled 3D auxetic cellular structures. *Materials & Design*, **99**, 467–76. DOI:[10.1016/j.matdes.2016.03.088](https://doi.org/10.1016/j.matdes.2016.03.088).
- Wang Z**, **Zhang Q**, **Zhang K** and **Hu G** (2016) Tunable Digital Metamaterial for Broadband Vibration Isolation at Low Frequency. *Advanced materials (Deerfield Beach, Fla.)*, **28**(44), 9857–61. DOI:[10.1002/adma.201604009](https://doi.org/10.1002/adma.201604009).
- Yang Z**, **Dai HM**, **Chan NH**, **Ma GC** and **Sheng P** (2010) Acoustic metamaterial panels for sound attenuation in the 50–1000 Hz regime. *Applied Physics Letters*, **96**(4), 41906. DOI:[10.1063/1.3299007](https://doi.org/10.1063/1.3299007).
- Zhang Z**, **Scarpa F**, **Bednarczyk BA** and **Chen Y** (2021) Harnessing fractal cuts to design robust lattice metamaterials for energy dissipation. *Additive Manufacturing*, **46**, 102126. DOI:[10.1016/j.addma.2021.102126](https://doi.org/10.1016/j.addma.2021.102126).
- Zhao J**, **Wang F**, **Zhang X**, **Liang L**, **Yang X**, **Li Q** and **Zhang X** (2018) Vibration Damping of Carbon Nanotube Assembly Materials. *Advanced Engineering Materials*, **20**(3), 1700647. DOI:[10.1002/adem.201700647](https://doi.org/10.1002/adem.201700647).
- Zhou XQ**, **Yu DY**, **Shao XY**, **Zhang SQ** and **Wang S** (2016) Research and applications of viscoelastic vibration damping materials: A review. *Composite Structures*, **136**, 460–80. DOI:[10.1016/j.compstruct.2015.10.014](https://doi.org/10.1016/j.compstruct.2015.10.014).
- Zschunke F** (2005) *Aktoren auf Basis des Magnetorheologischen Effekts. doctoral dissertation*, Erlangen: Erlangen-Nürnberg.
- Zschunke F**, **Rivas R** and **Brunn PO** (2005) Temperature Behavior of Magnetorheological Fluids. *Applied Rheology*, **15**(2), 116–21. DOI:[10.1515/arh-2005-0007](https://doi.org/10.1515/arh-2005-0007).